Journal of Power Sources 214 (2012) 266–276

Contents lists available at SciVerse ScienceDirect

Journal of Power Sources

journal homepage: www.elsevier.com/locate/jpowsour

Dynamic characterization of partially saturated engineered porous media and gas diffusion layers using hydraulic admittance

Perry Cheung, Joseph D. Fairweather, Daniel T. Schwartz*

University of Washington, Department of Chemical Engineering, Box 351750, Seattle, WA 98195-1750, USA

HIGHLIGHTS

- Performed hydraulic admittance on engineered porous sample with over 100 pores.
- Hydraulic admittance of engineered sample matched predicted simulation response.
- Performed hydraulic admittance on 2 GDL samples at different saturation states.
- Hydraulic admittance spectra of GDL samples show expected frequency dependence.
- Distinct resonance peaks show finite number of pores transport liquid water in GDL.

GRAPHICAL ABSTRACT

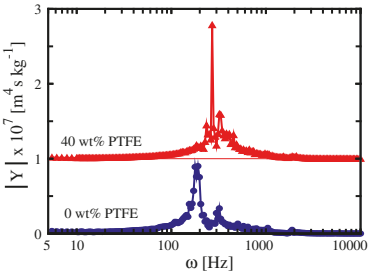

ARTICLE INFO

Article history:
Received 23 February 2012
Received in revised form
24 April 2012
Accepted 26 April 2012
Available online 8 May 2012

Keywords:
Polymer electrolyte membrane fuel cells
Liquid water distribution
Gas diffusion layers
Hydraulic admittance measurements
Capillary pressure measurements
Interfacial resonance

ABSTRACT

Simple laboratory methods for determining liquid water distribution in polymer electrolyte membrane fuel cell gas diffusion layers (GDLs) are needed to engineer better GDL materials. Capillary pressure vs. liquid saturation measurements are attractive, but lack the ability to probe the hydraulic interconnectivity and distribution within the pore structure. Hydraulic admittance measurements of simple capillary bundles have recently been shown to nicely measure characteristics of the free-interfaces and hydraulic path. Here we examine the use of hydraulic admittance with a succession of increasingly complex porous media, starting with a laser-drilled sample with 154 asymmetric pores and progress to the behavior of Toray TGP-H090 carbon papers. The asymmetric laser-drilled sample clearly shows hydraulic admittance measurements are sensitive to sample orientation, especially when examined as a function of saturation state. Finite element modeling of the hydraulic admittance is consistent with experimental measurements. The hydraulic admittance spectra from GDL samples are complex, so we examine trends in the spectra as a function of wet proofing (0% and 40% Teflon loadings) as well as saturation state of the GDL. The presence of clear peaks in the admittance spectra for both GDL samples suggests a few pore types are largely responsible for transporting liquid water.

1. Introduction

Polymer electrolyte membrane fuel cells (PEMFCs) are attractive as a power source due to high efficiency, low temperature, and low noise [1,2]. However, at high current densities the generated water condenses within the pores of the catalyst layer and underlying gas diffusion layer (GDL), and reduces the exposed

* Corresponding author. Tel.: +1 206 685 4815; fax: +1 206 685 3451/543 3778.
E-mail addresses: dts@u.washington.edu, dts@uw.edu (D.T. Schwartz).

0378-7753/$ – see front matter © 2012 Elsevier B.V. All rights reserved.
doi:10.1016/j.jpowsour.2012.04.088

catalyst surface area available for the electrochemical reaction [2–7]. To minimize disruption by liquid retention (flooding), the GDL pores must guide the formation of limited water pathways to the gas channels, so that additional liquid can be removed as it forms. GDLs typically have a thin hydrophobic microporous sublayer [8] and are treated with various Teflon loadings to render them hydrophobic [9–11]. The resulting GDL and microporous layer results in a complicated porous material with asymmetric wetting and hydraulic properties [12].

Based on the capillary number (Ca), which relates the viscous forces to surface tension forces, a fuel cell operating at 1 A cm^{-2} is dominated by capillarity with a Ca $\sim 10^{-8}$ [7,13] and falls under the capillary fingering regime (for more details on capillary fingering, refer to [14]). In light of this, there is now a movement toward pore-scale modeling that captures the liquid and gas structure within a pore-lattice network (see review [7]). Additionally, sophisticated imaging techniques (see review [15]) such as neutron radiography [16], magnetic resonance imaging, and synchrotron X-ray radiography [17–21] are continually making advances. Recently, Buchi's [19] group used X-ray tomographic microscopy to reconstruct both the solid GDL as well as the liquid water at different applied liquid water pressures with significantly improved spatial resolution. However, despite the improvement, the technique is still not readily available and currently limited to small GDL sample size of 2.5 mm in diameter, not the large areas normally found in stacks [21–24]. Despite the advances in imaging, sophisticated tools like these are geared toward fundamental understanding, not rapid lab-based materials development and optimization.

Capillary pressure vs. liquid saturation $P_C(S_L)$ measurements have been shown to be an attractive and straightforward characterization approach to quantify the hysteretic wetting of GDL samples during both liquid intrusion (where gas in the pores is displaced by liquid) and gas intrusion (where liquid in the pores is displaced by gas) [25–30]. However, this technique only probes the static interfacial curvature of all the hydraulically connected free-interfaces and lacks the ability to probe the characteristics of the hydraulic network leading to interfaces. Dimon et al. [31] developed a tool that could dynamically probe the interfacial resonance of a pinned free-interface in a single nearly full cylindrical capillary. When a small volumetric oscillation of frequency (ω) is dynamically applied to the pinned free-interface, an oscillatory pressure drop is generated. The complex, frequency dependent ratio of the applied volumetric displacement to this pressure drop is called the hydraulic admittance ($\tilde{Y}_{Hyd}(\omega)$). Using linear theory, the hydraulic admittance is the inverse sum of hydraulic impedances from viscous and inertial fluid forces in the filled part of the capillary ($\tilde{Z}_{V+I}(\omega)$), plus a capillary impedance ($\tilde{Z}_C(\omega)$) derived from the interface state

$$\tilde{Y}_{Hyd}(\omega) = -\frac{1}{\tilde{Z}_{V+I}(\omega)+\tilde{Z}_C(\omega)} \tag{1}$$

where

$$\tilde{Z}_{V+I}(\omega) = -\frac{\mu L(\omega/\omega_c)}{i\pi R^4\left[1-\frac{2}{\sqrt{i\omega/\omega_c}}\frac{J_1\left(\sqrt{i\omega/\omega_c}\right)}{J_0\left(\sqrt{i\omega/\omega_c}\right)}\right]} \tag{2}$$

$$\tilde{Z}_C(\omega) = \frac{2\gamma\sin(\theta)(1+\sin(\theta))^2}{i\omega\pi R^4} \tag{3}$$

and μ is dynamic viscosity of the fluid, L is the hydraulic path length, J_1 and J_0 are the 1st and zeroth order Bessel functions of the first kind, respectively, γ is the surface tension, and θ is the contact angle measured within the liquid. The characteristic frequency ω_c is defined by

$$\omega_c = \frac{\mu}{\rho R^2} \tag{4}$$

where ρ is the density of the fluid. When the magnitude of the hydraulic admittance is plotted against the applied oscillation frequency, resonance peaks are observed for every degenerate combination of fluid path and free-interface. The resonance frequency (ω_o) originates when the viscous and inertial impedances ($\tilde{Z}_{V+I}(\omega)$) are equal in magnitude to the capillary impedance ($\tilde{Z}_C(\omega)$) and 180° out of phase. The resonance frequency scales as

$$\omega_o \sim \sqrt{\frac{\gamma}{\rho R^2 L}} \tag{5}$$

To explore the potential of hydraulic admittance measurements as a probe for the hydraulic properties of complex porous media, we developed a bench-top tool [32] to accommodate porous samples that significantly extended previous studies of single nearly filled capillaries [31,33,34]. In order to accommodate different porous samples easily, the tool was designed to ensure Helmholtz resonances in the cavity did not interfere with the sample interfacial resonances [35–37]. Good agreement was found between theory and experiments for single capillaries and small bundles as a function of their fill state. Briefly, for a constant capillary radius, an increase in hydraulic path length results in a drop in hydraulic admittance magnitude and a shift toward lower frequencies, and for a constant hydraulic path length, an increase in the capillary radius results in an increase in hydraulic admittance magnitude and a shift toward lower frequencies. We further showed that the total hydraulic admittance ($\tilde{Y}_{Total}(\omega)$) of a bundle of M capillaries could be represented by

$$\tilde{Y}_{Total}(\omega) = \sum_{j=1}^{M}\tilde{Y}_{Hyd,j}(\omega) \tag{6}$$

for each individual admittance ($\tilde{Y}_{Hyd,j}(\omega)$). GDL materials are sometimes treated as a bundle of capillaries to approximate their more complex porous structure [4,29].

In this work, we expand our previous work by investigating the hydraulic admittance of more complex porous samples. We start with an engineered material that has hundreds of conical pores. Finite element modeling is included to understand the orientation dependence on the hydraulic admittance as a function of liquid saturations. We then take insights from quantitative measurements done here and previously to qualitatively explore the behavior of hydraulic admittance for two types of GDL samples. We focus on unique features of the measured admittance spectra and describe possible fluid displacement mechanisms that are consistent with the observed spectral features and previous work.

2. Methods

2.1. Materials

An acrylic (TAP plastics, Seattle, WA) porous sample was engineered by laser drilling (300-M Universal Laser Systems, Scottsdale, AZ) 154 pores as shown in Fig. 1. Several passes were necessary to drill all the way through, resulting in oblong-shaped pores instead of a perfect conical pore. Effective major and minor radii were measured from a series of images for both orientations. The effective pore radii reported here were calculated by equating the area of a circle to the area of an ellipse using the measured effective major and minor radii. The average contact angle of DI water on a smooth

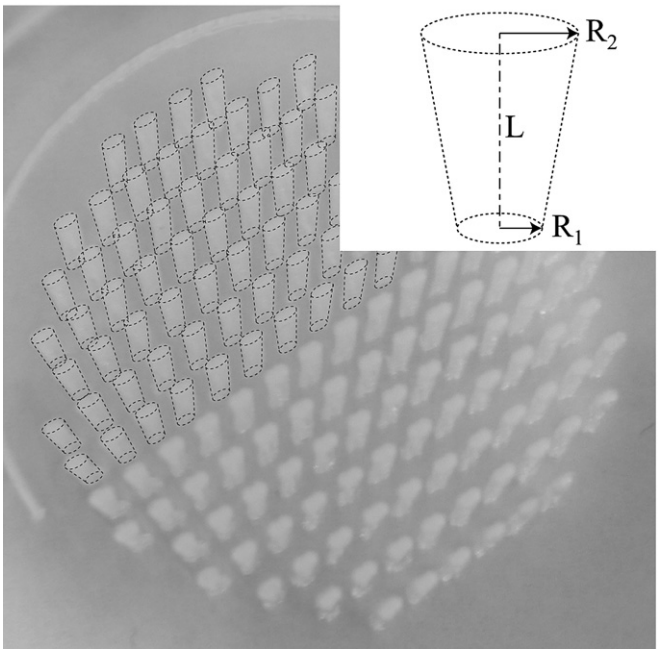

Fig. 1. Picture of the laser-drilled engineered porous sample (top down view).

acrylic surface was measured using a Rame-Hart model 100 contact angle goniometer. The effective properties of the acrylic pores are summarized in Table 1.

Two Toray TGP-H090 carbon papers with different Teflon loadings (0 wt% and 40 wt% Teflon loadings) were tested to determine the differences in the hydraulic admittance. The 0 wt% was left plain and the 40 wt% was commercially wetproofed by the supplier (BASF Fuel Cell, Somerset, NJ). The sample thickness was taken as the manufacturer-specified 280 μm. A thin ring of epoxy resin was impregnated at the edge of the 48 mm diameter GDL samples until a 28 mm exposed diameter was achieved to properly seal the GDL.

2.2. Finite element modeling

Two-dimensional axisymmetric flow fields were computed by fine element modeling using 3.3 Comsol multiphysics (Comsol, Los Angeles, CA) for geometries that represented the engineered porous sample. Two orientations of a single conical pore with effective pore dimensions were modeled to determine the influence of orientation and entrance effects on the hydraulic admittance. The model geometry and boundary conditions imposed are illustrated in Fig. 2. The value of R_o (effective pore spacing) was based on an equivalent radius of a circle that had the same area as the square array surrounding each pore. The inlet velocity was chosen such that the displacement length was 150 μm, an average maximum displacement length necessary for a pinned interface [31], at the smallest pore radii (R_1). Analytical manipulation of the Navier–Stokes equations allowed solution of the oscillating flow components with improved simulation efficiency, as detailed

Table 1
Effective properties of the acrylic pores.

Property	Value
L (mm)	11.96
R_1 (μm)	248
R_2 (μm)	424
θ (°)	61

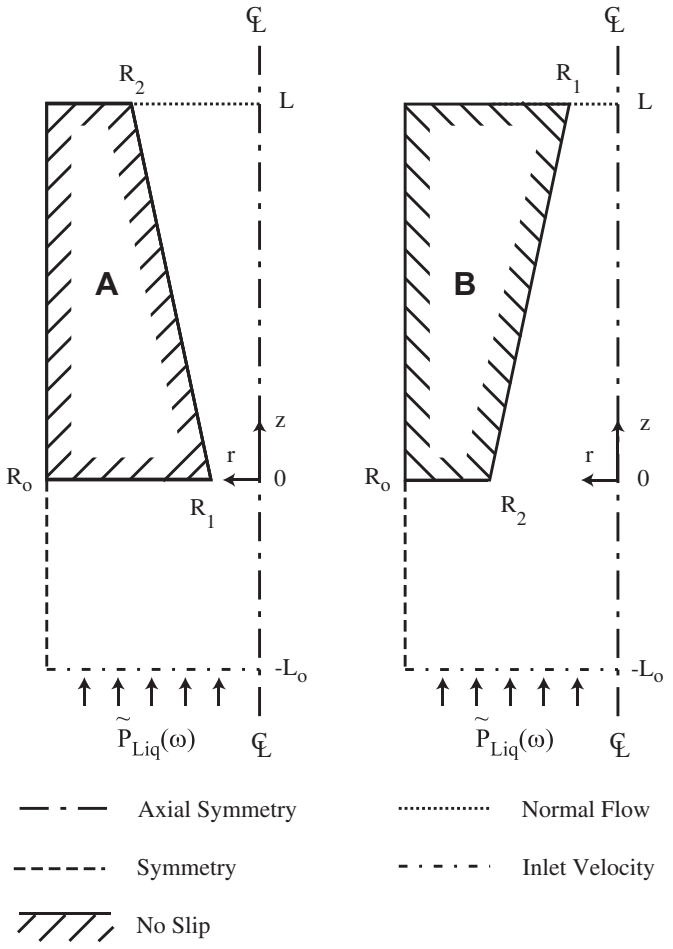

Fig. 2. A schematic of the two different geometries (A and B) used in the finite element modeling where R_o = 1.13 mm and L_o = 17 mm.

elsewhere [38]. Simulations were performed for a series of distinct oscillation frequencies. Viscous and inertial impedances were computed at discrete hydraulic path lengths (z) along the length of the pore by calculating the complex liquid pressure drop ($\tilde{P}_{Liq}(\omega)$) at the very bottom of the sample since the pressure was at a maximum and uniform with respect to the pressure drop in the pore. The hydraulic admittance was calculated using Eqn. (1) by analytically determining the capillary impedance using Eqn. (3) with the capillary radius determined geometrically at a hydraulic length z.

2.3. Dynamic capillary pressure vs. liquid volume measurements

Dynamic capillary pressure vs. liquid volume measurements were made to characterize the total wetting properties of the acrylic pores shown in Fig. 3A. The experimental procedure has been described previously [28–30]. A hydrophobic Teflon membrane (Pall Life Sciences TF-450, 0.45 μm characteristic pores) and hydrophilic Nylon membrane (Whatman NL 17, 0.45 μm characteristic pores) sandwiched the acrylic sample [28]. The hydrophobic membrane inhibited liquid water from breaking through the top of the sample during liquid intrusion by increasing the breakthrough pressure. Similarly, the hydrophilic membrane provided intimate contact with liquid water underneath the sample and inhibited air from exiting the bottom of the sample during gas intrusion by decreasing the bubble pressure. This

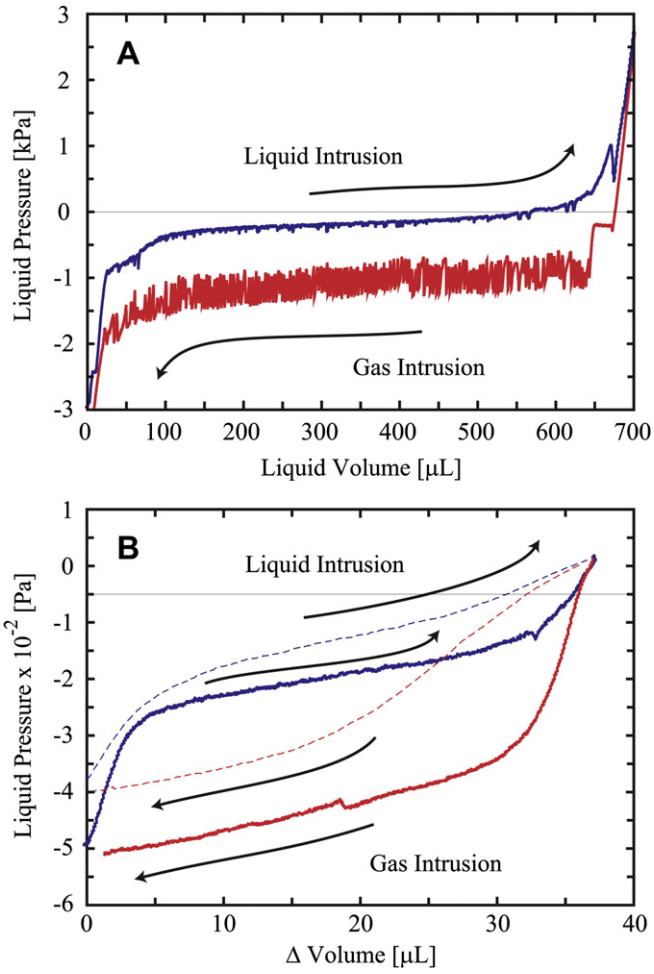

Fig. 3. (A) Dynamic capillary pressure vs. total liquid volume for orientation A. (B) Dynamic capillary pressure vs. ΔVolume for orientations A (dashed lines) and B (solid lines) for both liquid (blue) and gas intrusion (red). (For interpretation of the references to color in this figure legend, the reader is referred to the web version of this article.)

allowed the sample to be effectively saturated and drained despite varying capillary forces across the many parallel pathways in the sample. The hydrophobic membrane was completely dry and the hydrophilic membrane was completely saturated with liquid water for the pressure range used in the measurements, thus the measured static capillary pressures did not represent any liquid–air interfaces within the membranes. The acrylic sample was cycled multiple times at a rate at 5 μL min^{-1} until a repeatable curve was obtained.

2.4. Hydraulic admittance measurements

Fig. 4 shows an exploded view of the experimental tool that is composed of a series of acrylic layers (i–v). Briefly, a piezo diagraphm (D) is used to generate the oscillatory flow into the sample (B) with a known volumetric displacement. A reference layer (iii) comprised of a bundle of capillaries with known dimensions is positioned between a pair of pressure transducers (C) to determine the volumetric displacement. Several shut-off valves (A) are used to direct water into the tool, connect to a vacuum line, and allow equilibration to atmospheric pressure. A more detailed description of the tool, experimental procedure, and signal processing for the hydraulic admittance measurements has been

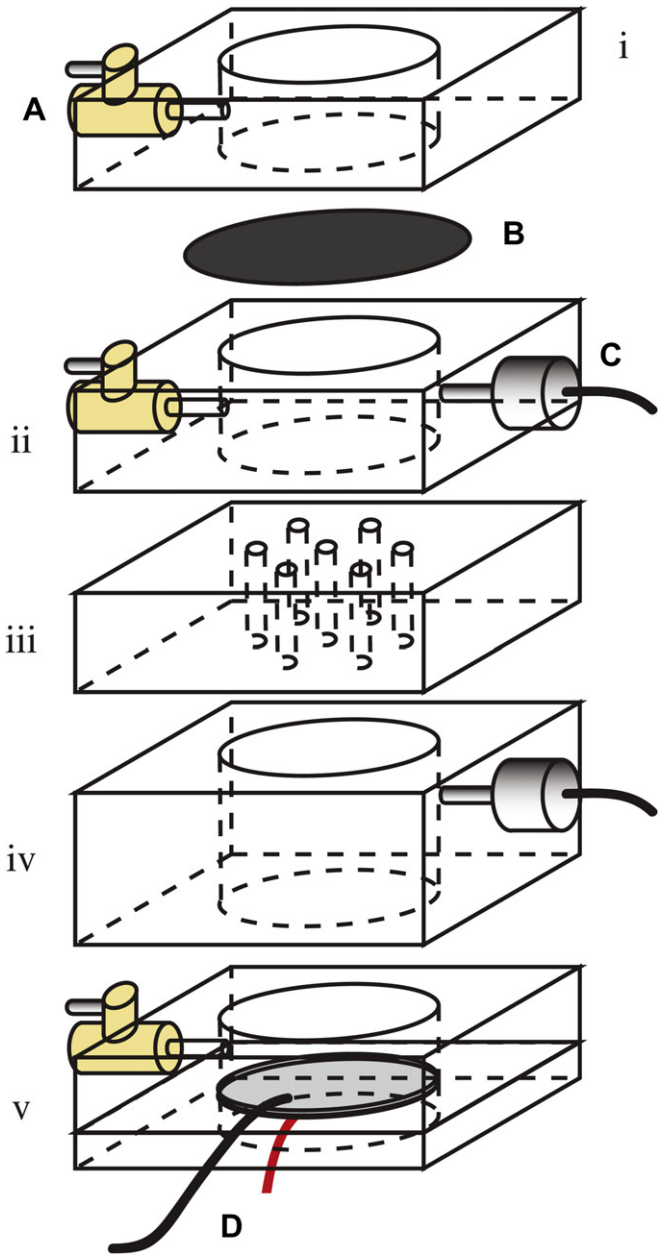

Fig. 4. An exploded view of the experimental tool used to measure the hydraulic admittance. The tool is assembled using a series of acrylic layers (i–v) and fluid valves (A), a sample (B), pressure transducers (C), and a piezo diaphragm (D).

described previously [32]. The use of any hydrophilic or hydrophobic membranes damped the hydraulic admittance response due to the increased hydraulic resistance in both liquid and gas phases, thus they were not used for any hydraulic admittance measurements. Hydraulic admittance measurements were performed on the acrylic sample in both orientations. For each orientation, a series of hydraulic admittance measurements were performed starting at a high ΔVolume along the gas intrusion curve shown in Fig. 3B, then reversed along the liquid intrusion curve until liquid breakthrough was achieved at a single pore. Upon liquid breakthrough, the liquid pressure dropped precipitously as the liquid bead grew until equilibrium was achieved. The liquid bead was then manually removed with a syringe, when possible. Due to the increased porosity of the acrylic sample, oscillation frequencies up to 1000 Hz were achieved without

interference from the Helmholtz resonance [36] previously reported [32].

The GDL samples were sealed with epoxy along the edge and were mounted into the hydraulic admittance tool also without the hydrophobic and hydrophilic membranes [28–30] because the membranes severely damped the hydraulic admittance of the sample. The samples were cycled with degassed DI water at a rate of 20.5 μL min^{-1} until liquid pressure vs. ΔVolume curves were consistent. The rate was chosen so the Ca was the same for liquid generation in an 80 °C PEFMC operated continuously at 1 A cm^{-2}. Hydraulic admittance measurements, similar to the acrylic sample, were performed first along the gas intrusion curve then along the liquid intrusion curve until liquid breakthrough was achieved. For the 40 wt% GDL sample, the bead of liquid water that formed was removed and liquid water was intruded back into the sample until breakthrough re-occurred at the same spot.

3. Results and discussion

3.1. Basic capillary properties of engineered sample

Based on the average pore dimensions in Table 1, the approximate total pore volume is about 668 μL and is consistent with Fig. 3A. One can count the number of liquid pressure jumps during gas intrusion, and it closely matches the number of pores. Thus, each liquid pressure jump is associated with a Haines jump [39] in each pore leading to complete drainage.

Dynamic capillary pressure vs. ΔVolume measurements made without the hydrophilic or hydrophobic membranes are shown in Fig. 3B for both orientations. Hydrophilic and hydrophobic membranes are used [28–30] in order to maximize the total accessible pores during gas and liquid intrusion, respectively, for capillary pressure measurements. Without either of these membranes, the cycled liquid pressure and volume were thus limited to a smaller range at the capillary pressures of lowest magnitude. The loop in Fig. 3B should therefore be compared to Fig. 3A in the approximate range of 500–540 μL. Based on the effective pore dimensions, the total ΔVolume cycled corresponds to probing about 10 pores. For the same amount of ΔVolume, we see that the dynamic capillary pressures are different between the two orientations. Clearly, the orientation has an effect on the observed wetting, where orientation A is less wetting than B since the dynamic capillary pressure curve is shifted toward higher values. For the same contact angle, this is expected given the pore geometry of orientations A and B.

3.2. Hydraulic admittance: finite element modeling

Computed hydraulic admittances for both orientations are shown in Fig. 5 for a series of hydraulic path lengths (i.e. interface positions) (i–vi). The admittance spectra for Fig. 5B have been sequentially shifted by 0.5×10^{-9} m^4 s kg^{-1} to see the resonance peaks more clearly. We see there is a significant difference between the two orientations in the hydraulic admittance as the hydraulic path length increases (i–vi). In orientation A, the resonance peak decreases in magnitude and shifts toward lower frequencies, while in orientation B, the resonance peak also decreases in magnitude but the peak position is relatively insensitive. The interpretation of the results is complicated for this geometry because the capillary radius is dependent on the hydraulic path length, whereas the capillaries previously investigated [32] had a constant radius.

If we consider the peak position for orientation A first, as both the hydraulic path length and radius increase (higher interface position), the resonance peak should shift toward lower frequencies. This dependence on hydraulic path length is consistent to

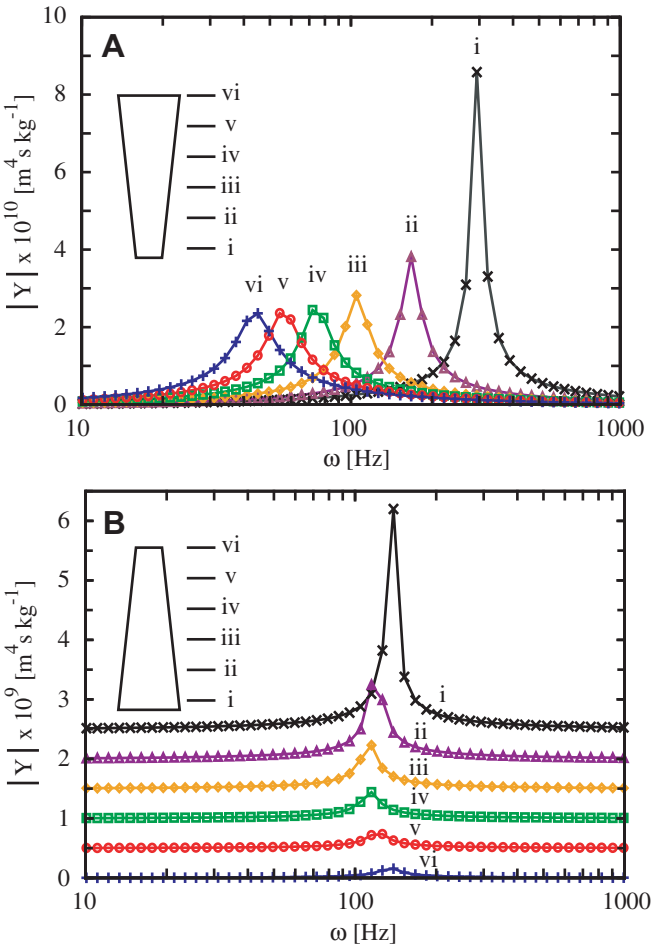

Fig. 5. Bode plots showing the magnitude of the hydraulic admittance at different interface positions (i–vi) for orientations A (A) and B (B) from the finite element modeling.

what was observed previously [32]. Let us now consider the peak magnitude. As the hydraulic path length is increased, $\tilde{Z}_{V+I}(\omega)$ will increase (lower admittance) resulting in a drop in the peak magnitude. However, as the capillary radius is increased, both $\tilde{Z}_{V+I}(\omega)$ and $\tilde{Z}_C(\omega)$ should decrease (increase in admittance). Because the change in capillary radius is insignificant with respect to the change in hydraulic path length, the peak magnitude is primarily controlled by the hydraulic path length. It is interesting to note that as the interface position moves up (i–vi) the difference in peak magnitudes decreases, that suggests the contribution from the increasing capillary radius will eventually dominate over the contribution from the increasing hydraulic length and produce an increasing peak magnitude.

For orientation B, let us consider the peak magnitude first. $\tilde{Z}_{V+I}(\omega)$ increases as the hydraulic path length increases, resulting in a decreased hydraulic admittance. For a decreasing capillary radius, both $\tilde{Z}_{V+I}(\omega)$ and $\tilde{Z}_C(\omega)$ will increase, resulting in a decreased hydraulic admittance. Thus, the peak magnitude should only decrease as the interface position moves up. Now let us consider the peak position. The peak position should shift toward lower frequencies as the hydraulic path length increases, for a given capillary radius, and should shift toward higher frequencies as the radius decreases, for a given hydraulic path length. Thus, there is a competing influence on the peak position due to increasing hydraulic path length and decreasing capillary radius as the interface position moves up. This phenomenon was not observed in

orientation A because the resonance peak shifted toward lower frequencies as the interface position moves up, since both hydraulic path length and radius increased.

3.3. Hydraulic admittance: engineered porous sample measurements

Fig. 6 shows the measured hydraulic admittance for the engineered sample in orientation A at various saturated states (i–x), with each state sequentially shifted up by 2×10^{-8} m^4 s kg^{-1}. Hydraulic admittance measurements were performed initially at a high ΔVolume (see Fig. 3B) (i) along the gas intrusion curve (i–iv) toward lower ΔVolume, then along the liquid intrusion curve (v–viii) toward increasing ΔVolume until a bead of water broke through at a pore (ix), and after removal of the bead (x). As

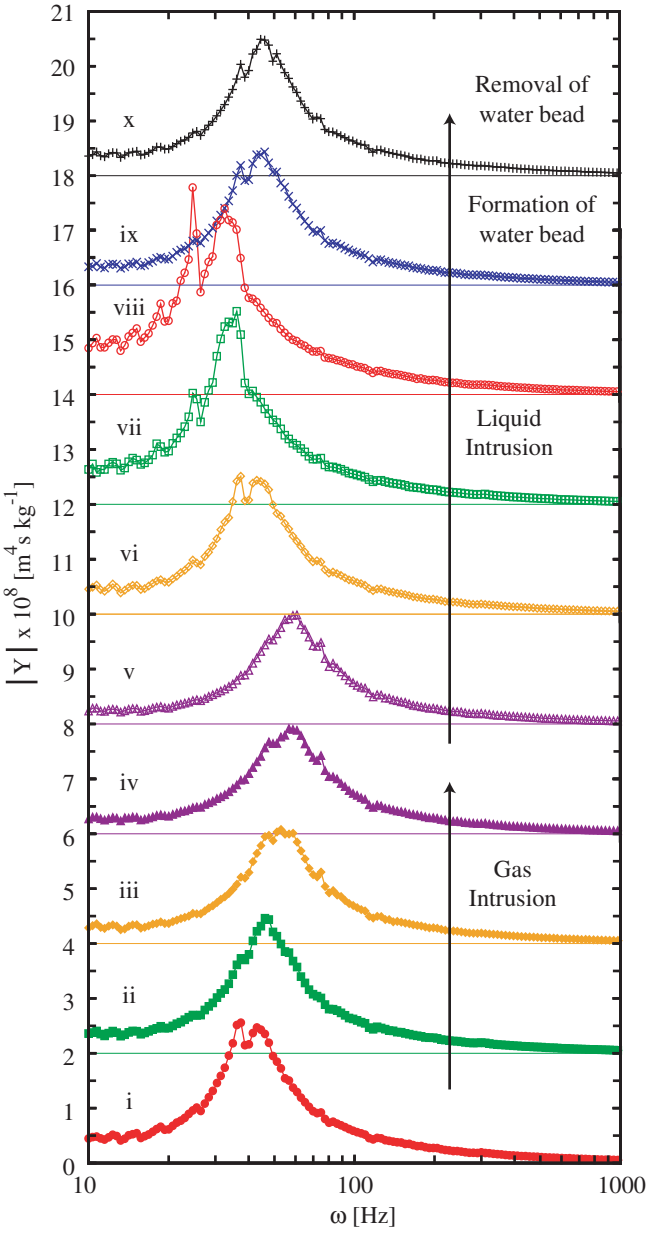

Fig. 6. Bode plots showing the magnitude of the measured admittance for orientation A starting along the gas intrusion curve (i–iv), continuing along the liquid intrusion curve (v–viii), until a bead of water breaks through (ix), and after its removal (x).

we move along the gas intrusion curve (i–iv) (equivalent to decreasing the hydraulic path length), the broad resonance feature decreases in magnitude and shifts toward higher frequencies with a slight broadening. Comparing this to Fig. 5A during gas intrusion (vi–i), we see that the shift toward higher frequencies matches the predicted response. However, the measured magnitude seems to decrease instead of increase as predicted. This apparent discrepancy can be explained by the 154 pores that make up the engineered sample. The observed resonance feature is a result from superimposing 154 individual resonance peaks, where each resonance peak can have different hydraulic path lengths as well as slightly different pore dimensions. The previous study [32] had shown the hydraulic admittance from each capillary within a capillary bundle adds linearly to generate the observed total hydraulic admittance. As the ΔVolume is decreased along the gas intrusion curve, only a finite number of pores are drained which leads to a decrease in their hydraulic path lengths. This decrease shifts the peak positions toward higher frequencies consistent with the model, while the remaining pores maintain the same hydraulic path length. Thus, the broad resonance feature becomes broader as some peaks shift toward higher frequencies while most of the peak positions remain the same, resulting in an apparent overall decrease in magnitude and broadening.

If we now consider the hydraulic admittance during liquid intrusion (v–vii), we see that the broad resonance feature becomes more narrow, increases in magnitude, and shifts toward lower frequencies as ΔVolume increases. Although we see an apparent discrepancy between the measured and predicted admittances, this again can be explained by the resonance peak shift from a finite number of pores. As the ΔVolume is increased along the liquid intrusion curve (equivalent to increasing hydraulic path length), only a finite number of pores begin to fill up which increases their hydraulic path lengths. This increase shifts a few resonance peak positions toward lower frequencies (consistent with the model) while the remaining pores maintain the same peak position. Thus, the originally broad resonance feature becomes less broad as some peaks shift toward lower frequencies while most of the peak positions remain the same, resulting in an apparent overall increase in magnitude and narrowing.

As the ΔVolume is increased further beyond the liquid intrusion curve, eventually the liquid breakthrough condition occurs and a bead of water forms at a single pore. The formation of the water bead drains some of the pores until the interfacial curvatures of all free-interfaces reach equilibrium or a snap-off condition occurs. When the hydraulic admittance is then measured again (ix), we see that there is a significant shift toward higher frequencies with a drop in magnitude. The shape of this broad resonance feature resembles the condition at (vi). Upon removal of the bead above the sample, we see that the hydraulic admittance remains the same. This suggests that snap-off occurred upon the formation of the liquid bead, since the removal of the bead did not produce a change in the measured admittance.

Fig. 7 shows the measured hydraulic admittance for the engineered sample in orientation B at various saturated states (i–x), with each state sequentially shifted up by 2×10^{-8} m^4 s kg^{-1}. The same hydraulic admittance measurements described for orientation A were performed for orientation B except the bead of water formed above the pore upon liquid breakthrough (x) could not be removed easily. As we move along the gas intrusion curve (i–iv) with decreasing ΔVolume, the broad resonance feature increases in magnitude but remains in the same position. Comparing this to Fig. 5B, we see that the resonance peak magnitude similarly increases as the hydraulic path length decreases with little change in peak position. The

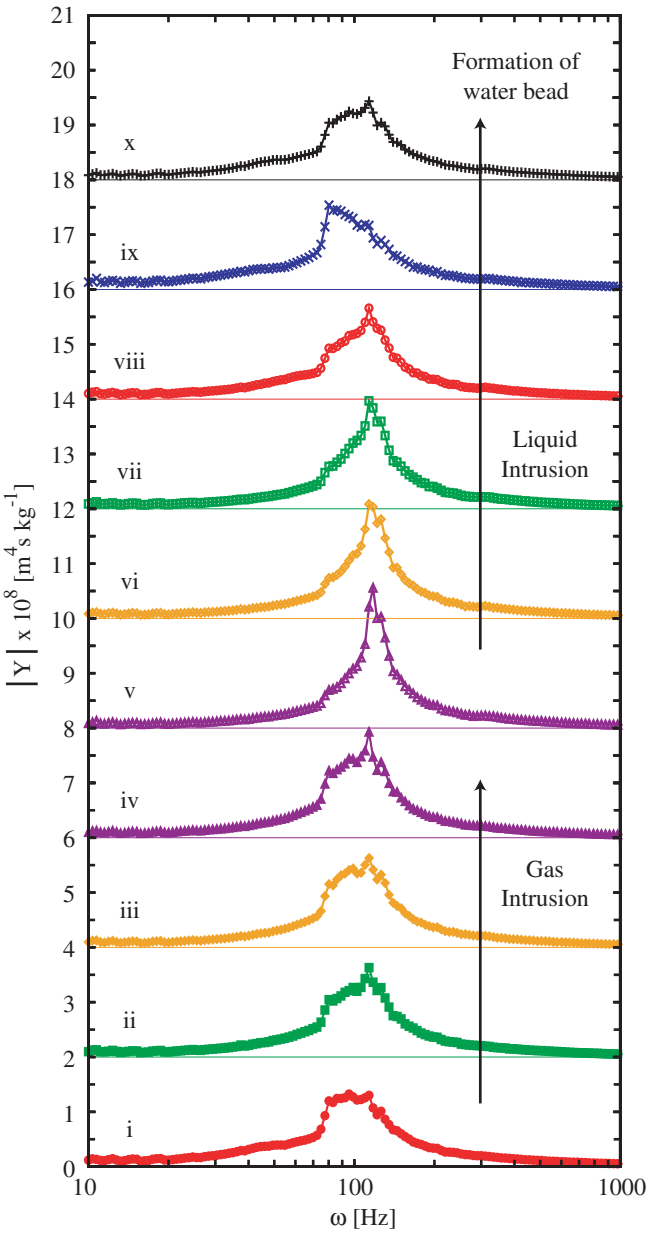

Fig. 7. Bode plots showing the magnitude of the measured admittance for orientation B starting along the gas intrusion curve (i–iv), continuing along the liquid intrusion curve (v–ix), and until a bead of water breaks through (x).

broad resonance feature appears to remain in the same position because only a finite number of peaks slightly shift in position with changes in the hydraulic path length.

Upon reversal to liquid intrusion, we see that the broad resonance feature deceases in magnitude but the position remains the same as the ΔVolume is increased. Again, this is consistent with the simulations and Fig. 5B. The admittance curve prior to liquid breakthrough (ix) is interesting in that there appears to be an apparent shift in the dominant resonance peak toward lower frequencies. This can be attributed by a finite number of peaks, such that the resulting admittance is accentuated within a narrow frequency range shifting toward lower frequencies. Upon liquid breakthrough (x), we see that the admittance curve shifts back to a curve that resembles (viii) due to the drop in hydraulic path length from the loss in volume.

3.4. Hydraulic admittance: GDL sample measurements

Fig. 8 shows the hydraulic admittance for both GDL samples at oscillation frequencies between 5 Hz and 10 kHz. This initial measurement was taken in order to determine the relevant frequency range with observable resonance peaks. All subsequent measurements were performed at frequencies between 100 Hz and 4000 Hz. We see that the resonance peaks for the 0 wt% GDL sample are centered at lower frequencies compared to the 40 wt% GDL. For a given hydraulic path length, larger capillary radii exhibit resonance peaks at lower frequencies, consistent with pore size distribution measurements [30] that show a smaller characteristic pore radii for the 40 wt% GDL sample compared to the 0 wt%. This decrease in pore radii can be attributed to Teflon coated carbon fibers.

Fig. 9 shows the measured hydraulic admittance for the 0 wt% PTFE GDL sample. Measurements were taken along the gas intrusion curve (i–iv), reversed along the liquid intrusion curve (v–x) until a bead of water formed (xi), and after its removal (xii). We clearly see there are a few prominent resonance peaks that exist at different levels of saturation (or capillary pressures). Specifically, measurements iii and vii show high resonance peaks at 112 Hz that dominate the entire spectra. Additionally, we see the same peaks (160 Hz, 276 Hz, and 330 Hz) show small changes in magnitude and are present prior to liquid breakthrough (x), after liquid breakthrough (xi), and upon removal of the bead of water (xii).

Fig. 10 shows the measured hydraulic admittance for the 40 wt% PTFE GDL sample. Measurements were taken along the gas intrusion curve (i–iv), reversed along the liquid intrusion curve (v–vii) until a bead of water formed (viii), and after its removal (ix). Upon removal of the bead, liquid water was intruded back into the GDL sample (x) until a bead of water formed again (xi) and then subsequently removed (xii). The bead of water that formed appeared in the same location each time, consistent to previous observations [5,6,40]. Similar to the 0 wt% GDL sample, we also see there are a few prominent resonance peaks that exist at different levels of saturation (capillary pressures). Again, we see the same peaks show slight changes in magnitude and are present prior to liquid breakthrough (vii and x), after liquid breakthrough (viii and xi), and upon removal of the bead of water (ix and xii).

For both spectra shown in Figs. 9 and 10, we see that only a finite number of peaks exist. This is similar to the spectra observed with a bundle of seven capillaries [32] and suggests that only a finite

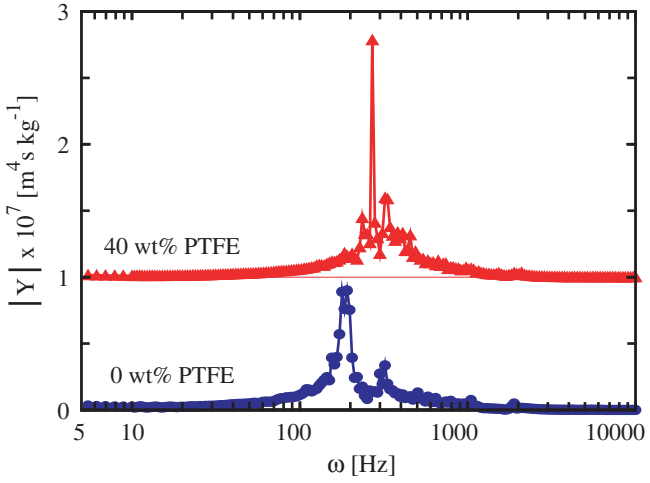

Fig. 8. Bode plot showing the magnitude of the measured admittance for the 0 wt% and 40 wt% PTFE GDL samples at an initial scan.

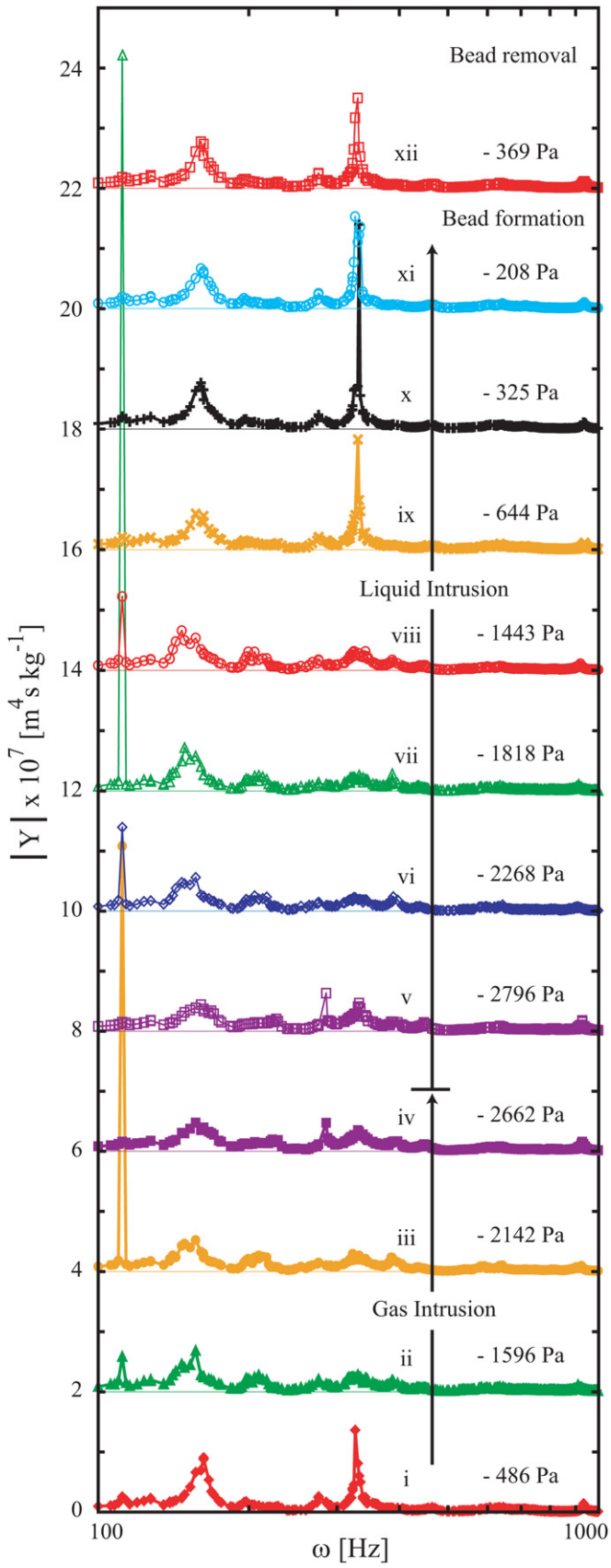

Fig. 9. Bode plots showing the magnitude of the measured admittance for the 0 wt% PTFE GDL sample measured along the gas intrusion curve (i–iv), along the liquid intrusion curve (v–x) until a bead of water breaks through (xi), and after its removal (xii). The capillary pressure was recorded before each measurement.

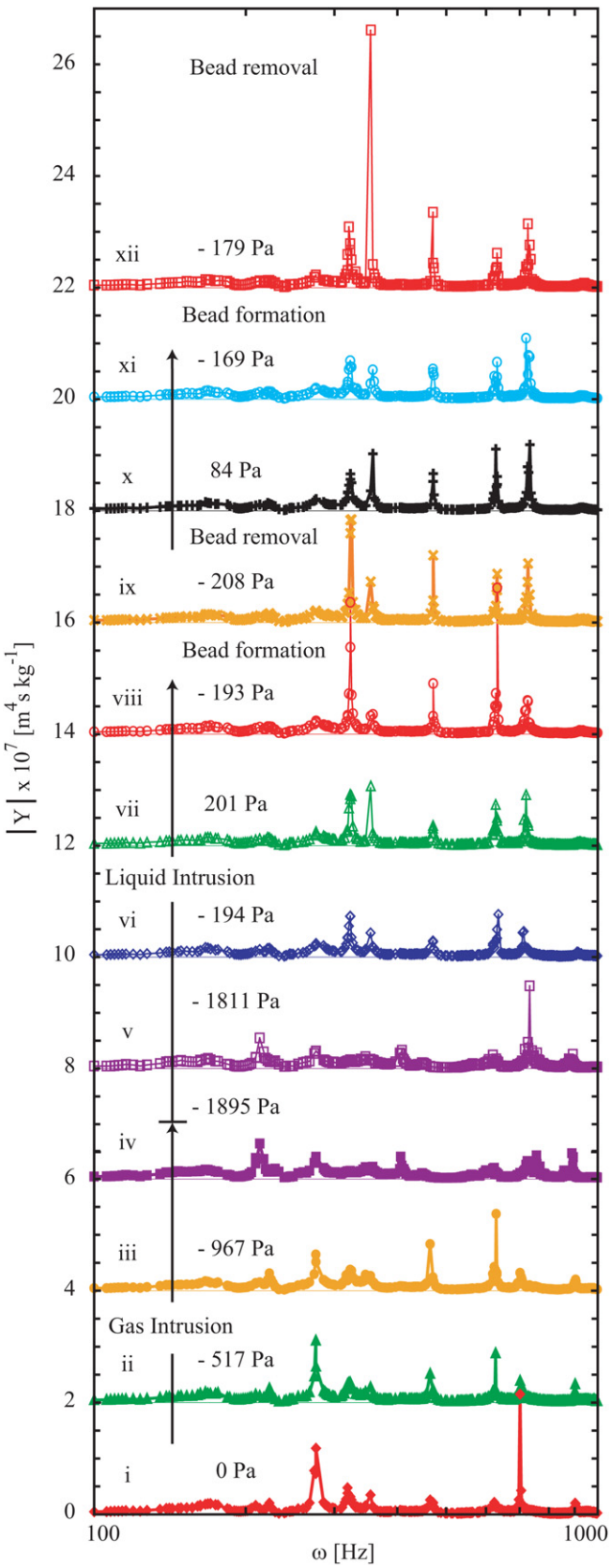

Fig. 10. Bode plots showing the magnitude of the measured admittance for the 40 wt% PTFE GDL sample measured along the gas intrusion curve (i–iv), along the liquid intrusion curve (v–vii) until a bead of water breaks through (viii), after its removal (ix), further liquid intrusion (x) until a bead of water breaks through again (xi), and after its removal (xii). The capillary pressure was recorded before each measurement.

number of pores with free-interfaces are involved in the displacement during liquid and gas intrusion. This is consistent with visualization studies that suggest a few pores transport the bulk of the liquid water [5,6,40].

Previous work with capillaries [32] had shown changes in hydraulic path length affect both the position and magnitude of the resonance peak. Figs. 11A and B show the dependence of the hydraulic admittance as a function of hydraulic path length and capillary radius, respectively using Eqns. (1)–(3). Fig. 11A shows the resonance peak decrease (i → iii) in magnitude and shift toward lower frequencies by doubling the hydraulic path lengths. Fig. 11B shows the resonance peak increase dramatically (i → iii) in magnitude and shift toward lower frequencies by doubling the capillary radii. These trends originate from the linear dependence on the hydraulic path length and 4th order inverse dependence on the capillary radius from $\tilde{Z}_{V+I}(\omega)$ and $\tilde{Z}_C(\omega)$ relationships, respectively. Although changes in hydraulic path length from changes in saturation affect both the magnitude and position of the resonance peaks, we would expect small but discernable changes. Since we are now dealing with a complex, tortuous, and highly connected network of pores, displacement mechanisms beyond changing hydraulic path lengths need to be considered. The remaining discussion focuses on these possible mechanisms that help explain the spectra observed in Figs. 9 and 10.

Figs. 12A and B show a cartoon of an interface being displaced to the right (i → iii) during liquid intrusion (or to the left (iii → i) during gas intrusion) and the corresponding hydraulic admittance, respectively. The hydraulic admittances were calculated using Eqns. (1)–(3) and ignore any entrance effects from the contraction and expansion. We see that the peak in configuration (ii) is shifted toward lower frequencies at about the same magnitude compared to the peak in configuration (i). The expansion of the pore radius (ii) shifts the resonance peak toward lower frequencies and also increases the magnitude due to the decrease in resistance (lower capillary impedance) while the increase in hydraulic path length decreases the magnitude slightly and shifts the peak to lower frequencies. As the displacement proceeds further toward configuration (iii), we see that the peak has shifted toward higher frequencies and has dropped in magnitude. This occurs because the capillary impedance is now the same as configuration (i) and the only difference is the increased hydraulic path length that shifts the peak toward a lower frequency and magnitude. Clearly, the act of displacing an interface into different pores with different capillary radii can have a dramatic effect on the peak position and magnitude. This displacement mechanism could possibly explain the sudden increase and subsequent drop in magnitude as observed in (iii) and (vii) in Fig. 9.

Fig. 13A and B shows a cartoon of two interfaces (i) merging (i → ii) during liquid intrusion (or one interface splitting (ii → i) during gas intrusion) to form a single interface (ii) and the corresponding hydraulic admittance spectra, respectively. The hydraulic admittance was calculated using Eqns. (1)–(3) and ignore any effects of having a junction. Initially, two resonance peaks (i) are

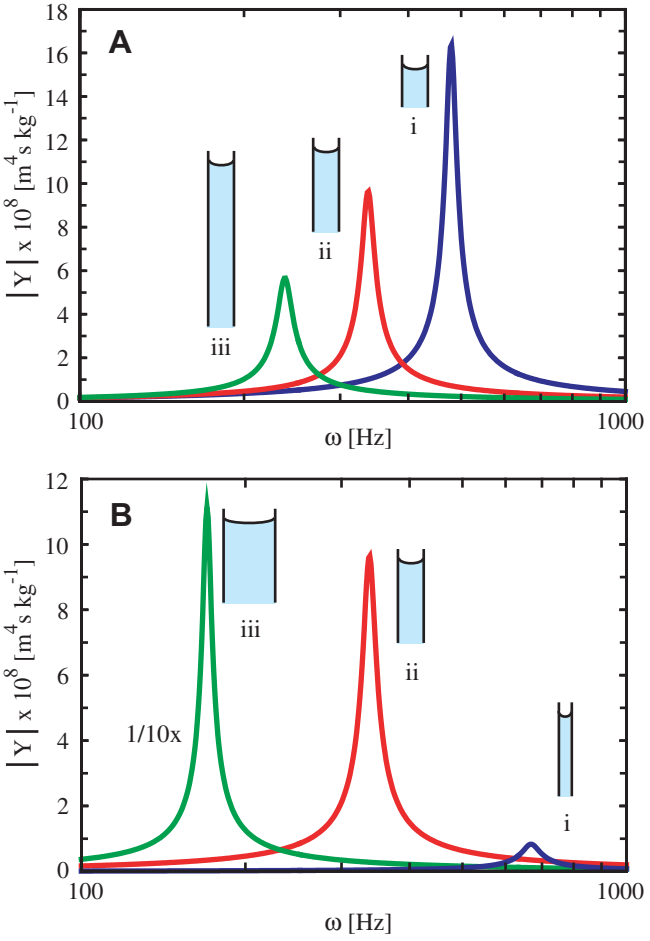

Fig. 11. Theoretical hydraulic admittance as a function of hydraulic path length (A). $R = 600$ μm, $\theta = 31°$, $L = 50$ μm (i), 100 μm (ii), and 200 μm (iii). Theoretical hydraulic admittance as a function of capillary radius (B). $R = 300$ μm (i), 600 μm (ii), and 1200 μm (iii), $\theta = 31°$, $L = 100$ μm.

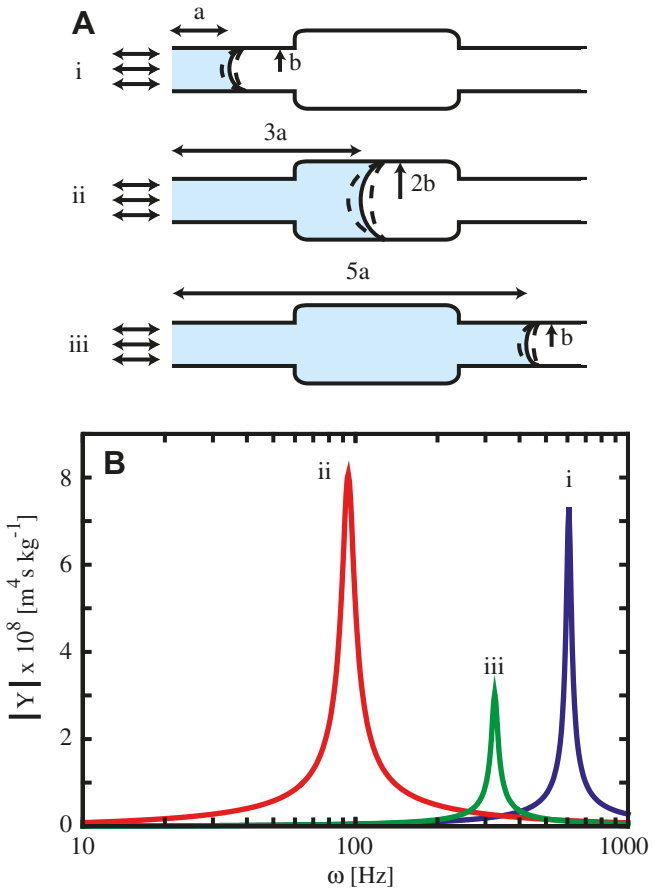

Fig. 12. (A) Cartoon of a fluid displacement mechanism involving an expansion (ii) and contraction in capillary radius (iii) using $a = 100$ μm, $b = 600$ μm, and $\theta = (80°, 70°,$ and $82°)$. (B) Theoretical hydraulic admittance spectra for the different interface positions (i–iii).

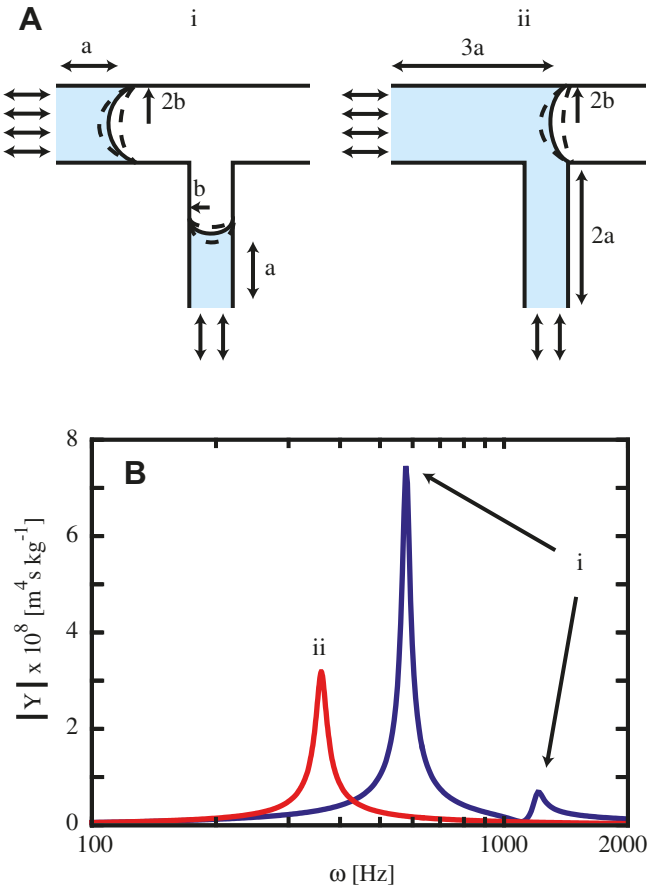

Fig. 13. (A) Cartoon of a fluid displacement mechanism that involves merging of two interfaces (liquid intrusion) or splitting of one interface (gas intrusion) using $a = 100$ μm, $b = 300$ μm, and $\theta = (80^\circ$ with b, 70° with $2b$, and 72° (ii)). (B) Theoretical hydraulic admittance spectra for the different interface positions (i–iii).

present with the peak at higher frequency and lower magnitude corresponding to the smaller pore, and the peak at lower frequency but higher magnitude corresponding to the larger pore. We see that once the two interfaces meet and merge to form a single interface, a single resonance peak (ii) is now observed. This new single peak is now both at a lower frequency and lower in magnitude (compared to the previous largest peak) due to the increase in hydraulic path length. The merging and splitting of interfaces at a junction can also explain the sudden appearance and disappearance of peaks at different saturations found in both Figs. 9 and 10. Additionally, because the number of interfaces has changed, this mechanism may explain any correlation among the appearance and disappearance of different resonance peaks.

Due to the complexity of the GDL material, quantitative analysis of the spectra observed in Figs. 9 and 10 cannot be performed at present. The fundamental issue is that water transport in the capillary fingering regime of fuel cells (and our experiments) is a percolation process, where small local differences in geometric and surface processes give rise to large effects in percolation path length and breakthrough (what we measure with our tool). This phenomenon is somewhat analogous to fracture statistics of brittle materials. In fracture statistics, a Weibull distribution is used to address the likelihood of specimen fracturing based on a weakest link hypothesis (i.e. the specimen fails if its weakest volume element fails) [41–43]. No single measurement of the ultimate yield strength of a brittle material, nor a small number of replicates, can provide a "characteristic" of the material. Instead, it is generally assumed that at least 30 specimens must be tested to assess the full Weibull distribution [41]. Similarly, fuel cell researchers studying water transport know there are special pores that drive water transport, and the literature is filled with descriptions of the role individual percolating pores play [5,6,40]. However, the position at which liquid breakthrough occurs or even when it occurs is something that cannot be predicted a priori because this event is driven by a series of small, random geometric and surface wetting differences. Thus, to properly describe "characteristic" pores that transport the bulk liquid water in a statistically meaningful way will require an extensive number of experiments.

4. Conclusions and implications

We have described here the ability to measure the hydraulic admittance for an engineered porous material that behaves very differently based simply on the orientation of the sample. The hydraulic admittance showed it is sensitive enough to discern the hydraulic and capillary differences in the orientation even for a large number of pores. Additionally, hydraulic admittance measurements can complement $P_C(S_L)$ measurements during both liquid and gas intrusion since the tool is capable of measuring the static liquid pressure prior to dynamic measurements, thus enabling simultaneous understanding of both the wetting and hydraulic properties of a porous material. When the hydraulic admittance measurements were repeated on the two GDL materials with different Teflon loadings, we observed the spectra for both samples contained only a finite number of sharp resonance peaks that suggest only a few pores are responsible for transporting water. Similar to the engineered acrylic sample, the spectra before liquid breakthrough are repeated upon liquid breakthrough which further suggest that transport of liquid water is dominated by a finite number of pores only and fills up in a cyclic fashion [40]. However, due to the complexity of the GDL material it is not possible at present to provide a statistically meaningful description of the "characteristic" pores that are responsible for transporting the bulk of the liquid water to the surface of the GDL.

Nonetheless, the bench-top tool we describe and demonstrate here is sufficiently easy to use and should be well-suited to carrying out statistically significant numbers of samples. Future work will involve exploring hydraulic admittances of simple interconnected pores in transparent materials to better understand the spectra observed in actual GDL materials as well as correlation of the observed spectra with simple visualization techniques [44].

Before further investigation of GDL materials using hydraulic admittance can be done, the additional resistance from hydrophobic and hydrophilic membranes needs to be addressed in order to fully probe the saturation states of GDLs [28–30]. The added resistance from these membranes prevents hydraulic admittance measurements with initially dry or fully saturated GDLs. Thus, membranes with high liquid breakthrough and bubblepoint pressures and also high permeability are necessary, but these two properties are mutually exclusive in commercially available membranes.

Acknowledgments

This work was supported in part by the Boeing-Sutter Endowment for Excellence in Engineering and National Science Foundation (NSF) (Grant No. DGE-0654252).

References

[1] K. Tüber, D. Pócza, C. Hebling, Journal of Power Sources 124 (2003) 403–414.
[2] C.Y. Wang, Chemical Reviews 104 (2004) 4727–4765.

[3] C.Y. Wang, Two-phase flow and transport, in: H.A.G. Wolf Vielstich, Arnold Lamm (Eds.), Handbook of Fuel Cells – Fundamentals, Technology and Applications, John Wiley & Sons, Ltd., 2003, pp. 337–347.
[4] A.Z. Weber, R.M. Darling, J. Newman, Journal of the Electrochemical Society 151 (2004) A1715–A1727.
[5] X.G. Yang, F.Y. Zhang, A.L. Lubawy, C.Y. Wang, Electrochemical and Solid State Letters 7 (2004) A408–A411.
[6] F.Y. Zhang, X.G. Yang, C.Y. Wang, Journal of the Electrochemical Society 153 (2006) A225–A232.
[7] P.K. Sinha, P.P. Mukherjee, C.Y. Wang, Journal of Materials Chemistry 17 (2007) 3089–3103.
[8] S. Litster, G. McLean, Journal of Power Sources 130 (2004) 61–76.
[9] M.F. Mathias, J. Roth, J. Fleming, W. Lehnert, Diffusion media materials and characterization, in: H.A.G. Wolf Vielstich, Arnold Lamm (Eds.), Handbook of Fuel Cells – Fundamentals, Technology and Applications, John Wiley & Sons, Ltd., New York, 2003.
[10] C. Lim, C.Y. Wang, Electrochimica Acta 49 (2004) 4149–4156.
[11] A.L. Dicks, Journal of Power Sources 156 (2006) 128–141.
[12] J.T. Gostick, M.A. Ioannidis, M.W. Fowler, M.D. Pritzker, Electrochemistry Communications 11 (2009) 576–579.
[13] P.K. Sinha, C.-Y. Wang, Electrochimica Acta 52 (2007) 7936–7945.
[14] R. Lenormand, Journal of Physics – Condensed Matter 2 (1990) SA79–SA88.
[15] A. Bazylak, International Journal of Hydrogen Energy 34 (2009) 3845–3857.
[16] R. Mukundan, R.L. Borup, Fuel Cells 9 (2009) 499–505.
[17] T. Sasabe, P. Deevanhxay, S. Tsushima, S. Hirai, Journal of Power Sources 196 (2011) 8197–8206.
[18] P. Kruger, H. Markotter, J. Haussmann, M. Klages, T. Arlt, J. Banhart, C. Hartnig, I. Manke, J. Scholta, Journal of Power Sources 196 (2011) 5250–5255.
[19] R. Fluckiger, F. Marone, M. Stampanoni, A. Wokaun, F.N. Buchi, Electrochimica Acta 56 (2011) 2254–2262.
[20] S.J. Lee, S.G. Kim, G.G. Park, C.S. Kim, International Journal of Hydrogen Energy 35 (2010) 10457–10463.
[21] H. Markötter, I. Manke, P. Krüger, T. Arlt, J. Haussmann, M. Klages, H. Riesemeier, C. Hartnig, J. Scholta, J. Banhart, Electrochemistry Communications 13 (2011) 1001–1004.
[22] K.S.S. Naing, Y. Tabe, T. Chikahisa, Journal of Power Sources 196 (2011) 2584–2594.
[23] K. Nishida, T. Murakami, S. Tsushima, S. Hirai, Journal of Power Sources 195 (2010) 3365–3373.
[24] D. Gerteisen, C. Sadeler, Journal of Power Sources 195 (2010) 5252–5257.
[25] C.R. Killins, R.F. Nielsen, J.C. Calhoun, Producers Monthly 18 (1953) 30–39.
[26] N.R. Morrow, Journal of Canadian Petroleum Technology (1976) 49–69.
[27] W.G. Anderson, Journal of Petroleum Technology 39 (1987) 1283–1300.
[28] J.D. Fairweather, P. Cheung, J. St-Pierre, D.T. Schwartz, Electrochemistry Communications 9 (2007) 2340–2345.
[29] P. Cheung, J.D. Fairweather, D.T. Schwartz, Journal of Power Sources 187 (2009) 487–492.
[30] J.D. Fairweather, P. Cheung, D.T. Schwartz, Journal of Power Sources 195 (2010) 787–793.
[31] P. Dimon, A.P. Kushnick, J.P. Stokes, Journal de Physique 49 (1988) 777–785.
[32] P. Cheung, J.D. Fairweather, D.T. Schwartz, Review of Scientific Instruments 82 (2011) 095102.
[33] E. Charlaix, H. Gayvallet, Journal de Physique II 2 (1992) 2025–2038.
[34] E. Charlaix, A.P. Kushnick, J.P. Stokes, Physical Review Letters 61 (1988) 1595–1598.
[35] P.M. Morse, K.U. Ingard, Theoretical Acoustics, McGraw-Hill, New York, 1968.
[36] P.K. Tang, W.A. Sirignan, Journal of Sound and Vibration 26 (1973) 247–262.
[37] P.M. Morse, Vibration and Sound, American Institute of Physics for the Acoustical Society of America, New York, 1981.
[38] J.A. Bowman, D.T. Schwartz, International Journal of Heat and Mass Transfer 41 (1998) 1065–1074.
[39] F.A.L. Dullien, Porous Media Fluid Transport and Pore Structure, Academic Press, New York, 1979.
[40] S. Litster, D. Sinton, N. Djilali, Journal of Power Sources 154 (2006) 95–105.
[41] R. Danzer, Journal of the European Ceramic Society 26 (2006) 3043–3049.
[42] J.B. Wachtmann, Mechanical Properties of Ceramics, John Wiley & Sons, New York, 1996.
[43] W. Weibull, Journal of Applied Mechanics – Transactions of ASME 18 (1951) 293–297.
[44] M. Shahraeeni, M. Hoorfar, Journal of Power Sources 196 (2011) 5918–5921.